VIRTUAL ANALOG BUCHLA 259 WAVEFOLDER

Fabián Esqueda, Henri Pöntynen, Vesa Välimäki

Acoustics Lab, Dept. of Signal Processing and Acoustics
Aalto University
Espoo, Finland
firstname.lastname@aalto.fi

Julian D. Parker

Native Instruments GmbH
Berlin, Germany
julian.parker@native-instruments.com

ABSTRACT

An antialiased digital model of the wavefolding circuit inside the Buchla 259 Complex Waveform Generator is presented. Wavefolding is a type of nonlinear waveshaping used to generate complex harmonically-rich sounds from simple periodic waveforms. Unlike other analog wavefolder designs, Buchla's design features five op-amp-based folding stages arranged in parallel alongside a direct signal path. The nonlinear behavior of the system is accurately modeled in the digital domain using memoryless mappings of the input–output voltage relationships inside the circuit. We pay special attention to suppressing the aliasing introduced by the nonlinear frequency-expanding behavior of the wavefolder. For this, we propose using the bandlimited ramp (BLAMP) method with eight times oversampling. Results obtained are validated against SPICE simulations and a highly oversampled digital model. The proposed virtual analog wavefolder retains the salient features of the original circuit and is applicable to digital sound synthesis.

1. INTRODUCTION

To talk about Don Buchla is to talk about the history of the analog synthesizer. Motivated by his early experiments with musique concrète, California native Donald "Don" Buchla was drawn to the San Francisco Tape Music Center in 1963, where he began collaborating with composers Morton Subotnick and Ramon Sender [1]. Subotnick and Sender commissioned Buchla to design a voltage-controlled musical instrument that could manipulate the characteristics of sounds generated by function generators. This led to the development of Buchla's first synthesizer, the Buchla 100 [1, 2], completed in 1964.

From the beginning, Buchla's approach to sound synthesis was fundamentally different to that of his contemporaries, particularly Robert Moog. In Moog synthesizers, sounds are sculpted by filtering harmonically-rich waveforms with resonant filters. This method is known in the literature as "subtractive" synthesis and is commonly dubbed "East Coast" synthesis as a reference to Moog's New York origins. In contrast, Buchla's synthesis paradigm (known as "West Coast" synthesis) concentrates on timbre manipulation at oscillator level via nonlinear waveshaping, frequency modulation or phase locking. A trademark module in Buchla synthesizers is the lowpass gate, a filter/amplifier circuit capable of producing acoustic-like plucked sounds by using photoresistive opto-isolators, or "vactrols", in its control path [3]. Buchla's designs played a key role in the development of electronic music and can be heard across numerous recordings, such as in the works of the renowned composer Suzanne Ciani [4].

Recent years have seen a resurgence of interest in analog synthesizers, with music technology powerhouses such as Moog and Korg re-releasing modern versions of their now classic designs. Similarly, contemporary manufacturers of modular synthesizers like Make Noise, Sputnik Modular and Verbos Electronics, to name a few, have reinterpreted Buchla's designs, rekindling the interest in analog West Coast synthesis. This rise in popularity serves as the motivation to study classic analog devices and to develop virtual analog (VA) models which can be used within digital audio environments. VA instruments are generally more affordable than their analog counterparts, and are exempt from issues such as electrical faults and component aging [5].

In this work we present a novel VA model of the timbre circuit inside the seminal Buchla 259, a complex waveform generator released in 1970 as part of the Buchla 200 synthesizer. The 259 is a dual oscillator module with frequency modulation and waveform synchronization capabilities that provide a wide timbral palette. However, its most distinctive feature is its wavefolding circuit capable of producing the rich harmonic sweeps characteristic to West Coast synthesis. Wavefolding is a type of nonlinear waveshaping in which parts of the input signal that exceed a certain value are inverted or "folded back". This process introduces high levels of harmonic distortion and thus alters the timbre of the signal.

The use of nonlinear distortion to generate complex sounds has been widely studied within the context of digital synthesis. Well-known methods include the use of nonlinear waveshaping functions, such as Chebyshev polynomials, to expand the spectrum of simple sinusoids [6–9], and frequency modulation (FM) synthesis [10]. Other methods include modified FM synthesis [11], bitwise logical modulation and vector phaseshaping synthesis [12, 13]. Previous research on VA modeling of nonlinear analog audio systems has covered a wide spectrum of topics, including Moog's ladder filter [14–18], other nonlinear filters [3, 19–21], distortion circuits [22–26] and effects units [27–29].

One of the major challenges in VA modeling is to minimize the effects of aliasing distortion. Aliased components are known to be perceptually disturbing and unpleasant, but become negligible if attenuated sufficiently [30, 31]. The brute force method to reduce aliasing is oversampling, but, if the nonlinearity introduces high levels of distortion, the sample rate may have to be very high to obtain good audio quality. Aliasing suppression techniques have been thoroughly studied in the field of digital audio synthesis [32–35] and, more recently, in nonlinear audio processing [36–39]. In this work we propose the use of the previously introduced bandlimited ramp (BLAMP) method [36, 37] which can be used to bandlimit the corners, or edges, introduced by the wavefolding operation. The BLAMP method significantly reduces the oversampling requirements of the system.

This paper is organized follows. Section 2 details the analysis of the circuit. Section 3 deals with its implementation in the digital domain with emphasis on aliasing suppression. Finally, results and concluding remarks are presented in Sections 4 and 5, respectively.

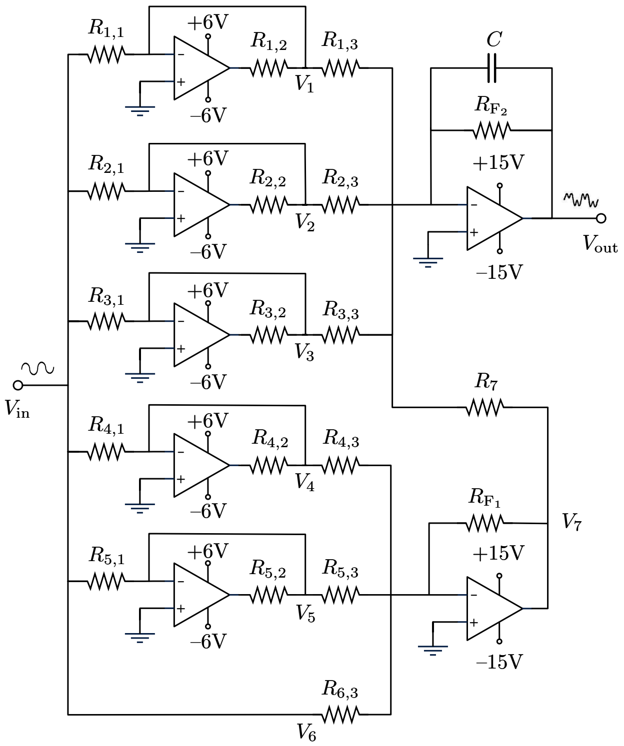

Figure 1: *Simplified schematic of the Buchla 259 timbre circuit.*

2. CIRCUIT ANALYSIS

Figure 1 shows a simplified schematic of the Buchla 259 timbre circuit. This figure has been adapted from Andre Theelen's DIY version of the circuit [1]. The main difference between Fig. 1 and Buchla's original design[2] is the omission of the "Symmetry" and "Order" controls, which are not considered in this study. The following treatment of the circuit adheres, for the most part, to the analysis presented by Prof. Aaron Lanterman as part of his lecture series "Electronics for Music Synthesis" [40].

The wavefolder inside the Buchla 259 consists of five non-identical op-amp-based folding cells arranged in parallel alongside a direct signal path, as shown in Fig. 1. The two op-amps on the right-hand side of the schematic are set up as summing amplifiers and are used to combine the outputs of all six branches. Overall, this parallel topology differs from that of the more common transistor/diode-based wavefolders, where multiple folding stages are usually cascaded together, e.g. as in the middle section of the Serge Wave Multipliers[3]. The Intellijel μFold II[4] and Toppobrillo Triple Wavefolder[5] are examples of commercially-available designs built around a series topology.

To simplify the analysis of the circuit, we first derive the input–output voltage relationship of a single folding cell. Since the parallel paths share the same structure, this result can be applied to all folding branches. Component values for the circuit are given in Table 1. Indices have been used to indicate branch number, e.g. $R_{5,2}$ denotes resistor R_2 in the fifth branch.

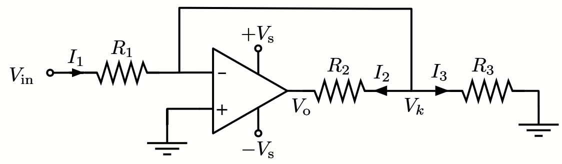

Figure 2: *Circuit diagram for a single folding cell, cf. Fig. 1.*

2.1. Single Folding Cell

Figure 2 shows the schematic for an op-amp circuit that is in the context of this work referred to as a folding cell. The variable V_{in} represents the voltage appearing at the input of all six branches. In the Buchla 259 the input of the timbre circuit is wired internally to the output of a sinusoidal oscillator. We denote the output voltage of each folding branch by V_k, where k is the branch number as counted from top to bottom. The value V_{o} denotes the voltage at the output terminal of the op-amp. Since R_3 is connected to the virtual ground node formed at the inverting input terminal of the succeeding summing amplifier (see Fig. 1), we assume loading effects between the branches to be minimal, and thus treat each folding cell individually.

First, we assume ideal op-amp behavior and apply Kirchhoff's voltage law (KVL). This results in the current–voltage relationships

$$V_{\text{in}} = R_1 I_1 + V_{\text{k}} \qquad \text{and} \qquad V_{\text{o}} = V_{\text{k}} - R_2 I_2, \tag{1}$$

where

$$V_{\text{k}} = R_3 I_3. \tag{2}$$

Rearranging these equations in terms of currents then gives us

$$I_1 = \frac{V_{\text{in}} - V_{\text{k}}}{R_1}, \quad I_2 = \frac{V_{\text{k}} - V_{\text{o}}}{R_2} \quad \text{and} \quad I_3 = \frac{V_{\text{k}}}{R_3}. \tag{3}$$

Next, we apply Kirchhoff's current law (KCL) at node V_{k} to establish the current relation

$$I_1 = I_2 + I_3. \tag{4}$$

Plugging (3) into (4) results in the expression

$$\frac{V_{\text{in}} - V_k}{R_1} = \frac{V_k - V_{\text{o}}}{R_2} + \frac{V_{\text{k}}}{R_3}, \tag{5}$$

Table 1: *Component values for the Buchla 259 circuit in Fig. 1.*

Name	Value	Name	Value	Name	Value
$R_{1,1}$	10 kΩ	$R_{1,2}$	100 kΩ	$R_{1,3}$	100 kΩ
$R_{2,1}$	49.9 kΩ	$R_{2,2}$	100 kΩ	$R_{2,3}$	43.2 kΩ
$R_{3,1}$	91 kΩ	$R_{3,2}$	100 kΩ	$R_{3,3}$	56 kΩ
$R_{4,1}$	30 kΩ	$R_{4,2}$	100 kΩ	$R_{4,3}$	68 kΩ
$R_{5,1}$	68 kΩ	$R_{5,2}$	100 kΩ	$R_{5,3}$	33 kΩ
–	–	C	100 pF	$R_{6,3}$	240 kΩ
R_7	24.9 kΩ	R_{F_1}	24.9 kΩ	R_{F_2}	1.2 MΩ

[1] www.ecalpemos.nl/sdiy/buchlaesque-modular/mutant-259-timbre-modindex-section/

[2] rubidium.dyndns.org/~magnus/synths/companies/buchla/

[3] http://www.cgs.synth.net/modules/cgs52_folder.html

[4] www.intellijel.com/eurorack-modules/μfold-ii/

[5] www.toppobrillo.com/TWF/TWF.html

which we can solve for V_k as:

$$V_\text{k} = \frac{R_3\left(R_2 V_\text{in} + R_1 V_\text{o}\right)}{R_1 R_3 + R_2 R_3 + R_1 R_2}. \tag{6}$$

Now, since the op-amp is in the inverting configuration, the value of V_o is defined as

$$V_\text{o} = -\frac{R_2}{R_1} V_\text{in}. \tag{7}$$

This definition implies that the op-amp can provide a fixed gain of $-\frac{R_2}{R_1}$ for all values of V_in. If we were to substitute (7) into (6) we would find that $V_k = 0$, as required by ideal op-amp behavior (i.e., the op-amp maintains the input terminals at the same potential) [41]. In practice, however, the value of V_o is limited by the supply voltages and the device is unable to maintain V_k at ground potential when the input voltage is high. Note that the op-amps in the folding branches are connected to lower supply voltages than the rest of the circuit.

Buchla's original design utilized CA3160 op-amps in its folding cells. This particular "rail-to-rail" op-amp features a CMOS output stage and is capable of swinging the output up to the supply voltages. As illustrated in its datasheet [42], the CA3160 exhibits a sharp saturating behavior similar to hard clipping. Therefore, we rewrite (7) as

$$V_\text{o} = \begin{cases} -\frac{R_2}{R_1} V_\text{in}, & \text{if} \quad |V_\text{in}| \leq \frac{R_1}{R_2} V_\text{s} \\ -\text{sgn}\left(V_\text{in}\right) V_\text{s}, & \text{otherwise}, \end{cases} \tag{8}$$

where $V_\text{s} = 6\,\text{V}$ is the supply voltage of the op-amp and sgn() is the *signum* function.

By combining (6) and (8), we can derive a piecewise expression for the output of each folding branch in the original circuit:

$$V_k = \begin{cases} \dfrac{R_{k,3}\left(R_{k,2} V_\text{in} - \text{sgn}(V_\text{in}) R_{k,1} V_\text{s}\right)}{R_{k,1} R_{k,3} + R_{k,2} R_{k,3} + R_{k,1} R_{k,2}}, & \text{if}\, |V_\text{in}| > \frac{R_{k,1}}{R_{k,2}} V_\text{s} \\ 0, & \text{otherwise}. \end{cases} \tag{9}$$

Figures 3(a)–(e) show the value of V_{1-5} for values of V_in between –10 V and 10 V measured at 1 mV steps using SPICE. Since no publicly available SPICE model for the CA3160 seems to exist, LTC6088 was used in the simulations instead. This device is similar to the CA3160 in that it also features a "rail-to-rail"-capable CMOS output stage [43]. These plots show that the output of each folding cell has a "deadband" in the input voltage region where the op-amp displays ideal behavior and maintains V_k at ground potential. At larger input voltage values, the op-amp output saturates to the supply voltage and is unable to maintain the deadband.

2.2. Mixing Stages

Following the folding cells, the output voltages of the six parallel branches are combined with two inverting amplifiers. Voltage V_7, the output of the lower amplifier (cf. Fig. 1), is formed as the weighted sum of the voltages from the three lower branches

$$V_7 = -R_{\text{F}_1}\left(\frac{V_4}{R_{4,3}} + \frac{V_5}{R_{5,3}} + \frac{V_\text{in}}{R_{6,3}}\right). \tag{10}$$

This voltage is subsequently fed to the input of the upper amplifier along with voltages V_{1-3}. The upper amplifier is an active first-order integrator that lowpass filters the weighted combination of the input signals. Assuming that the op-amp is operating within its linear region, the summing and filtering operations commute. Therefore, we can simplify the analysis by representing this stage as an inverting amplifier cascaded with a first-order lowpass filter. By replacing capacitor C with an open circuit we can then derive an expression for V'_out, the output of the circuit before filtering:

$$V'_\text{out} = -R_{\text{F}_2}\left(\frac{V_1}{R_{1,3}} + \frac{V_2}{R_{2,3}} + \frac{V_3}{R_{3,3}} + \frac{V_7}{R_7}\right). \tag{11}$$

Figure 4(a) shows a SPICE simulation of the input–output voltage relation of the entire circuit when the output filter is bypassed. It can be seen that the weighted sum of the individual branches (cf. Fig. 3) implements a piecewise linear waveshaping function. Figure 4(b) illustrates the outcome of driving the circuit with a sinusoidal signal. A fundamental frequency of 100 Hz and a peak voltage of 5 V were used in this simulation. The output of the circuit exhibits high levels of harmonic distortion which dramatically alters its timbral characteristics. In general, the output signal is perceived as harsher than the original input signal. Significant timbral variation can be achieved by simply modulating the amplitude of the input sinusoid. The filtering effect of the upper summing amplifier is discussed in Section 3.1.

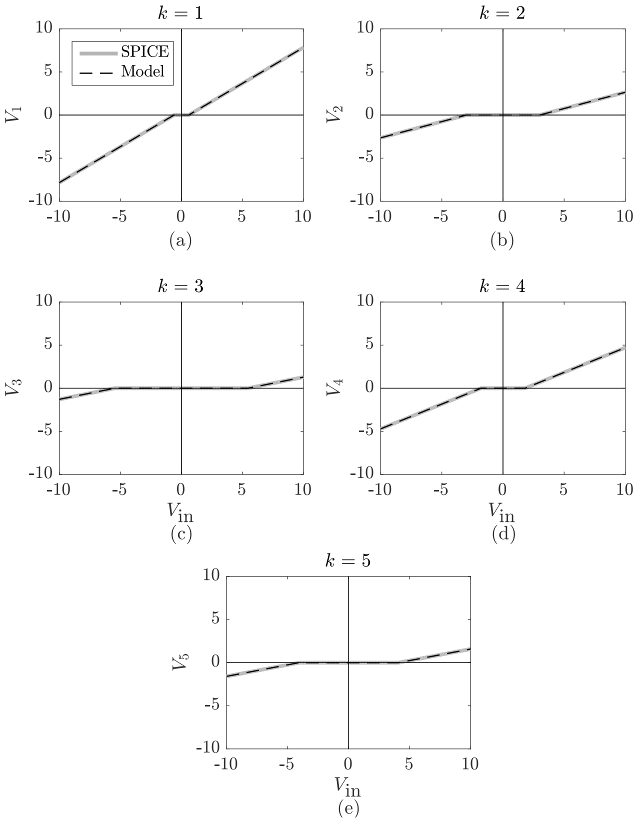

Figure 3: *SPICE simulation of the input–output voltage relation of each folding branch against the proposed digital mappings.*

3. DIGITAL IMPLEMENTATION

With the exception of the filtering stage at the output, the Buchla 259 timbre circuit can be categorized as a static system. This

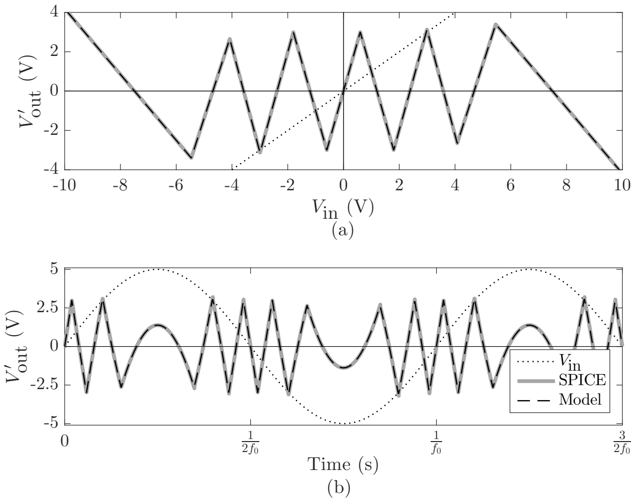

Figure 4: *Comparison of the input–output relationship of a SPICE simulation of the Buchla 259 timbre circuit and the proposed digital model for (a) a DC voltage sweep and (b) 100-Hz sinusoidal input with 5-V peak gain.*

means that we can derive a digital model using discrete memoryless mappings of the voltage relationships derived in the previous section. First, we define our discrete-time sinusoidal input as

$$V_{\text{in}}[n] = A\sin(2\pi f_0 nT), \tag{12}$$

were n is the sample index, A is peak amplitude, f_0 is the fundamental frequency and T is the sampling period, i.e. $T = 1/f_{\text{s}}$.

From (9) we can then define explicit discrete-time expressions for the output of each folding branch. To facilitate their implementation, terms containing resistor values have been evaluated and replaced for their corresponding approximate scalar values:

$$V_1[n] = \begin{cases} 0.8333V_{\text{in}}[n] - 0.5000s[n] & |V_{\text{in}}[n]| > 0.6000 \\ 0, & \text{otherwise,} \end{cases} \tag{13}$$

$$V_2[n] = \begin{cases} 0.3768V_{\text{in}}[n] - 1.1281s[n] & |V_{\text{in}}[n]| > 2.9940 \\ 0, & \text{otherwise,} \end{cases} \tag{14}$$

$$V_3[n] = \begin{cases} 0.2829V_{\text{in}}[n] - 1.5446s[n] & |V_{\text{in}}[n]| > 5.4600 \\ 0, & \text{otherwise,} \end{cases} \tag{15}$$

$$V_4[n] = \begin{cases} 0.5743V_{\text{in}}[n] - 1.0338s[n] & |V_{\text{in}}[n]| > 1.8000 \\ 0, & \text{otherwise,} \end{cases} \tag{16}$$

$$V_5[n] = \begin{cases} 0.2673V_{\text{in}}[n] - 1.0907s[n] & |V_{\text{in}}[n]| > 4.0800 \\ 0, & \text{otherwise,} \end{cases} \tag{17}$$

where $s[n] = \operatorname{sgn}(V_{\text{in}}[n])$. From these branches we can then define a global summing stage:

$$\begin{aligned} V'_{\text{out}}[n] \; = \; & -12.000V_1[n] - 27.777V_2[n] - 21.428V_3[n] \\ & +17.647V_4[n] + 36.363V_5[n] + 5.000V_{\text{in}}[n]. \end{aligned} \tag{18}$$

Figures 3 and 4 show the input–output relation of these mappings against the previously presented SPICE simulations. These results show a good match between the original and modeled behavior, with an absolute error in the range of 10^{-5} V.

3.1. Filtering Stage

The filter at the output of the system is a one-pole lowpass filter. In the Laplace domain, the transfer function of this filter is given by

$$H(s) = \frac{w_{\text{c}}}{s + w_{\text{c}}}, \tag{19}$$

where $w_{\text{c}} = 2\pi f_{\text{c}}$ and f_{c} represent the cutoff frequency in radians and Hz, respectively [44,45]. From Fig. 1 the cutoff of the filter is derived as

$$f_{\text{c}} = \frac{1}{2\pi R_{\text{F}_2} C} \approx 1.33\,\text{kHz}. \tag{20}$$

This relatively low cutoff frequency indicates the purpose of the filter is simply to act as a fixed tone control, attenuating the perceived brightness of the output by introducing a gentle 6-dB/octave roll-off. Equation (19) can be discretized using the bilinear transform, which results in the z-domain transfer function

$$H(z) = \frac{b_0 + b_1 z^{-1}}{1 + a_1 z^{-1}}, \tag{21}$$

where

$$b_0 = b_1 = \frac{w_{\text{c}}T}{2 + w_{\text{c}}T} \qquad \text{and} \qquad a_1 = \frac{w_{\text{c}}T - 2}{w_{\text{c}}T + 2}.$$

Due to the low cutoff parameter, the warping effects of the bilinear transform can be neglected. This transfer function can be implemented digitally, e.g. using Direct Form II Transposed [44].

3.2. Antialiasing

Given the highly nonlinear nature of wavefolding, audio-rate implementations of the proposed model using (12)–(18) will suffer from excessive aliasing distortion. This problem can be attributed to the corners or edges introduced by the folding cells of the system (cf. Fig. 4). These corners indicate that the first derivative of the signal is discontinuous and, as such, has infinite frequency content. In the discrete-time domain, frequency components that exceed the Nyquist limit will be reflected into the audio band as aliases.

To ameliorate this condition we propose the use of the BLAMP method, which has previously been used in the context of ideal nonlinear operations such as signal clipping and rectification [36, 37]. This method consists of replacing the corners with bandlimited versions of themselves. It is an extension of the bandlimited step (BLEP) method used in subtractive synthesis [33–35], which is in turn based on the classic bandlimited impulse train (BLIT) synthesis method [32].

The BLAMP function is a closed-form expression that models a bandlimited discontinuity in the first derivative of a signal. It is derived from the second integral of the bandlimited impulse [35], or sinc, function and is defined as

$$R_{\text{BL}}(t) := t\left[\frac{1}{2} + \frac{1}{\pi}\text{Si}(\pi f_{\text{s}} t)\right] + \frac{\cos(\pi f_{\text{s}} t)}{\pi^2 f_{\text{s}}}, \tag{22}$$

where t is time and $\text{Si}(x)$ is the sine integral

$$\text{Si}(x) := \int_0^x \frac{\sin(t)}{t}\text{d}t. \tag{23}$$

Computing the difference between the BLAMP and the ideal ramp function

$$R(t) := \begin{cases} t, & \text{when } t \geq 0 \\ 0, & \text{when } t < 0 \end{cases} \tag{24}$$

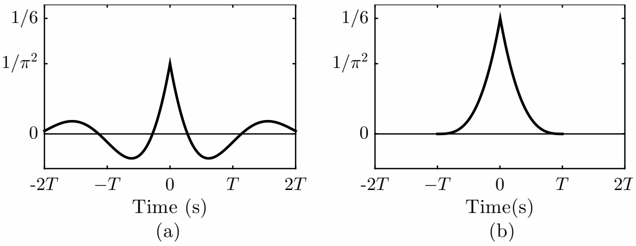

Figure 5: *Time domain representation of (a) the central lobe of the BLAMP residual function and (b) its two-point polynomial approximation.*

produces the BLAMP residual function shown in Fig. 5(a). In the discrete-time domain, this function is used to reduce aliasing by superimposing it on every corner within the waveform and sampling it at neighboring sample points. A crucial step in this process is centering the residual around the exact point in time where each discontinuity occurs, which is usually between samples.

Due to the high computational costs of evaluating (22), we will use its two-point polynomial approximation (polyBLAMP) instead [36]. Figure 5(b) illustrates the time-domain waveform of the two-point polyBLAMP residual function evaluated using the expressions given in Table 2. In this context $d \in [0, 1)$ is the fractional delay required to center the residual function between two samples.

In the case of the Buchla 259 timbre circuit, the BLAMP method is applied independently within each folding branch. To facilitate its implementation, we define an intermediate processing step in which the input–output relationships of the folding cells (13)–(17) are rewritten as inverse clippers. We then denote the output of the kth inverse clipper as V'_k, which can be written as

$$V'_k[n] = \begin{cases} V_{\text{in}}[n], & \text{if } |V_{\text{in}}[n]| > \dfrac{R_{k,1}}{R_{k,2}} V_{\text{s}} \\ \operatorname{sgn}(V_{\text{in}}[n]) \dfrac{R_{k,1}}{R_{k,2}} V_{\text{s}}, & \text{otherwise.} \end{cases} \tag{25}$$

Figure 6 shows the input–output relation of this intermediate processing stage. The advantage of this seemingly unnecessary step is that now we can apply the BLAMP method following the same approach described in [36] and [37] for the case of the regular hard clipper. This process involves detecting the transition from non-clipping to clipping samples (i.e. detecting the corners), computing the exact fractional clipping point and adding the correction function to the samples immediately before and after each corner. Prior to addition, the polyBLAMP function must be scaled by the slope of the input signal at the clipping point. Since we know the input to the system is a sinusoidal waveform, we can compute the fractional clipping points and their respective slopes analytically, thus facilitating the implementation and improving the robustness of the method.

Table 2: *Two-point polyBLAMP function and its residual [36].*

Span	Two-point polyBLAMP $d \in [0, 1)$
$[-T, 0]$	$d^3/6$
$[0, T]$	$-d^3/6 + d^2/2 + d/2 + 1/6$
Span	Two-point polyBLAMP residual $d \in [0, 1)$
$[-T, 0]$	$d^3/6$
$[0, T]$	$-d^3/6 + d^2/2 - d/2 + 1/6$

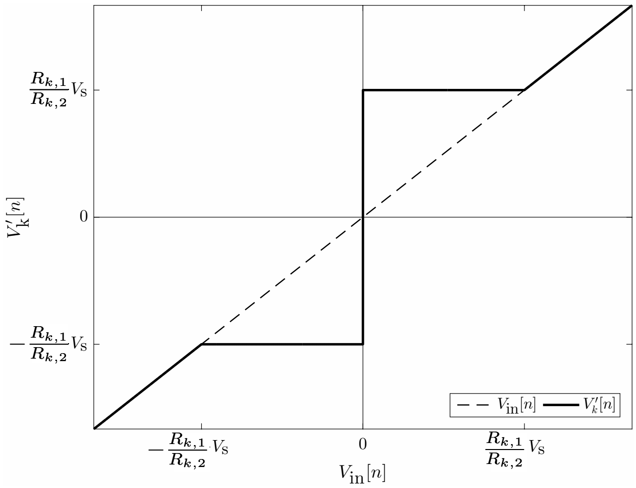

Figure 6: *Input–output relationship of the proposed intermediate processing step, the inverse clipper* (25).

For an arbitrary inverse clipper stage (25) driven by an f_0-Hz sinewave starting at zero phase, the first clipping point (in seconds) is given by

$$t_1 = \frac{\sin^{-1}(V_{\text{s}} R_{k,1}/A R_{k,2})}{2\pi f_0}. \tag{26}$$

From this value, we can evaluate the three remaining clipping points within the first period of the signal:

$$t_2 = \frac{1}{2f_0} - t_1, \quad t_3 = \frac{1}{2f_0} + t_1 \quad \text{and} \quad t_4 = \frac{1}{f_0} - t_1. \tag{27}$$

Figure 7(a) shows the result of inverse-clipping the first period of a sinewave, all four clipping points are highlighted. Subsequent clipping points can then be computed by adding multiples of the fundamental period, i.e. $1/f_0$.

For a stationary sinewave, the magnitude of the slope is the same at all clipping points. Therefore, we can define a closed-form expression of the polyBLAMP scaling factor as

$$\mu = |2\pi f_0 A \cos(2\pi f_0 t_{1-4}) / f_{\text{s}}|. \tag{28}$$

Figure 7(b) illustrates the process of centering the polyBLAMP residual function at each clipping point, scaling it and sampling it at neighboring samples. The polarity must be adjusted according to the polarity of the signal at the clipping point. Although in this study we only consider the case of sinusoidal inputs, the same approach can be adapted when other periodic signals are used as input to the wavefolder, e.g. sawtooth and triangular waveforms.

Now, if we then define $\widetilde{V}'_k$ as the signal that results from applying the polyBLAMP method to V'_k, we can write an expression for $\widetilde{V}_k$, the antialiased output of each folding cell:

$$\widetilde{V}_k[n] = \frac{R_{k,2} R_{k,3}}{R_{k,1} R_{k,3} + R_{k,2} R_{k,3} + R_{k,1} R_{k,2}} \Bigg[\widetilde{V}'_k[n] - \operatorname{sgn}\left(\widetilde{V}'_k[n]\right) \frac{V_{\text{s}} R_{k,1}}{R_{k,2}} \Bigg]. \tag{29}$$

This step basically undoes the intermediate processing step (25) while preserving the antialiased behavior.

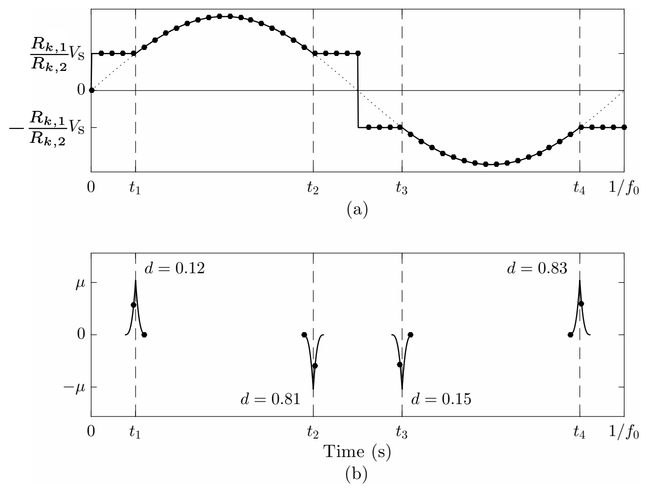

Figure 7: *(a) Time-domain representation of a sinewave processed by the inverse clipping stage* (25) *and (b) the process of centering the polyBLAMP residual at each clipping point. The fractional delay is given for each corner.*

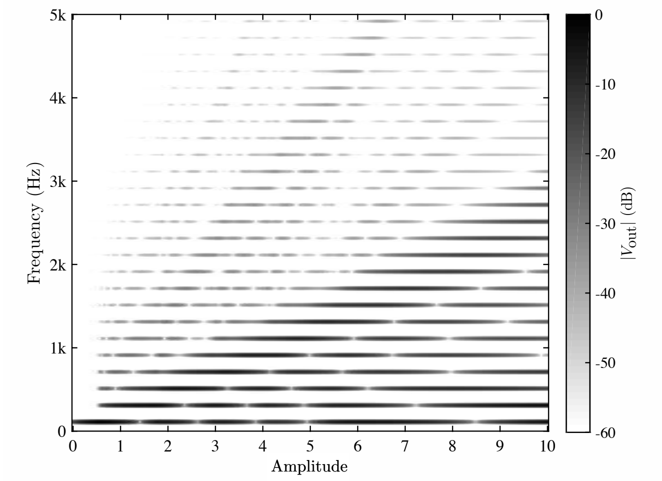

Figure 8: *Magnitude response of the system for a 110-Hz sinusoidal input with amplitude ranging from 0 to 10.*

A complete block diagram of the proposed wavefolder model, including the output filter, is given in Fig. 9. Boxes labeled $w_{1-5}()$ consist of the inverse clipper (25) followed by polyBLAMP correction and the mapping function (29). Once again, a tilde has been used to distinguish $\widetilde{V}_{\mathrm{out}}$, the output of the system with aliasing suppression, from V_{out}, its trivial counterpart.

4. RESULTS

Having compared the time-domain characteristics of the proposed model against SPICE simulations (cf. Figs. 3 and 4), in this section we move on to observe and evaluate its frequency-domain behavior. The spectrogram in Fig. 8 shows the effect of sweeping the input gain A from 0 to 10 for a sinewave with fundamental frequency $f_0 = 100\,\mathrm{Hz}$. Compared to typical saturating waveshapers (e.g. the tanh function or the hard clipper), where the level of introduced harmonics is directly proportional to input gain, wavefolding generates complex harmonic patterns reminiscent of FM synthesis. From a perceptual point of view, the folded waveform can be described as being brighter and more abrasive than the original input signal. It should be pointed out that due to the odd symmetry of the wavefolding operation [cf. Fig. 4(a)], the system introduces odd harmonics only.

Next, we analyze the effect of wavefolding on a static 890-Hz input sinewave with amplitude $A = 5$. Figures 10(a)–(b) show the waveform and magnitude spectrum, respectively, of the system's output when implemented at audio rate (i.e. $f_s = 44.1\,\mathrm{kHz}$) and without polyBLAMP correction. The resulting signal is practically unusable, as it exhibits very high levels of audible aliasing distortion. In comparison, Figs. 10(c)–(d) show the outcome of operating at the same rate but employing the two-point polyBLAMP method. As expected, the overall level of aliasing has been considerably attenuated. Next, Figs. 10(e)–(f) show the output of the system for a sample rate $f_s = 2.82\,\mathrm{MHz}$, i.e. 64 times the previous rate. This example was generated by synthesizing the input sinewave at the target rate and plotting only those frequency components below 20 kHz. The output is virtually free from aliasing, with only a handful of components laying above the –100 dB line. Lastly, Figs. 10(g)–(h) show the outcome of using eight times oversampling and the proposed polyBLAMP method. Results obtained are comparable to those in Fig. 10(f), which indicates that the proposed method reduces the oversampling requirements of the system.

The overall increase in signal quality provided by the two-point polyBLAMP method was measured for a larger set of input signals. Figure 11 shows the measured signal-to-noise ratio (SNR) at the output of the wavefolder for input sinewaves with fundamental frequency between 100 Hz and 5 kHz. In this context, we consider SNR to be the power ratio between the desired harmonics and aliasing components. This plot shows that the two-point polyBLAMP method provides an SNR increase of approx. 12 dB over a trivial audio-rate implementation. When combined with eight times oversampling the proposed method yields an average SNR increase of approx. 20 dB w.r.t. oversampling by factor 64.

In terms of computational costs, the two-point polyBLAMP method is highly efficient in that only samples around discontinuities are processed. Therefore, the complexity of the method increases as a function of fundamental frequency, not oversampling factor. For the case of a 5-kHz sinusoidal input (i.e. the worst-case scenario for the polyBLAMP method in terms of operation count), Matlab simulations indicated that the proposed method is approx. 6 times faster than oversampling by factor 64. This estimate does not include the costs of any resampling filters at the output of the system, which will also be more expensive for the case of oversampling by 64. An implementation of the proposed model and accompanying sound examples are available at `http://research.spa.aalto.fi/publications/papers/dafx17-wavefolder`.

5. CONCLUSIONS

In this work we have examined the underlying structure of the Buchla 259 wavefolder, also known as the timbre circuit. The analysis of the circuit provides a glimpse into the unconventional designs of Don Buchla and his approach to sound synthesis. A digi-

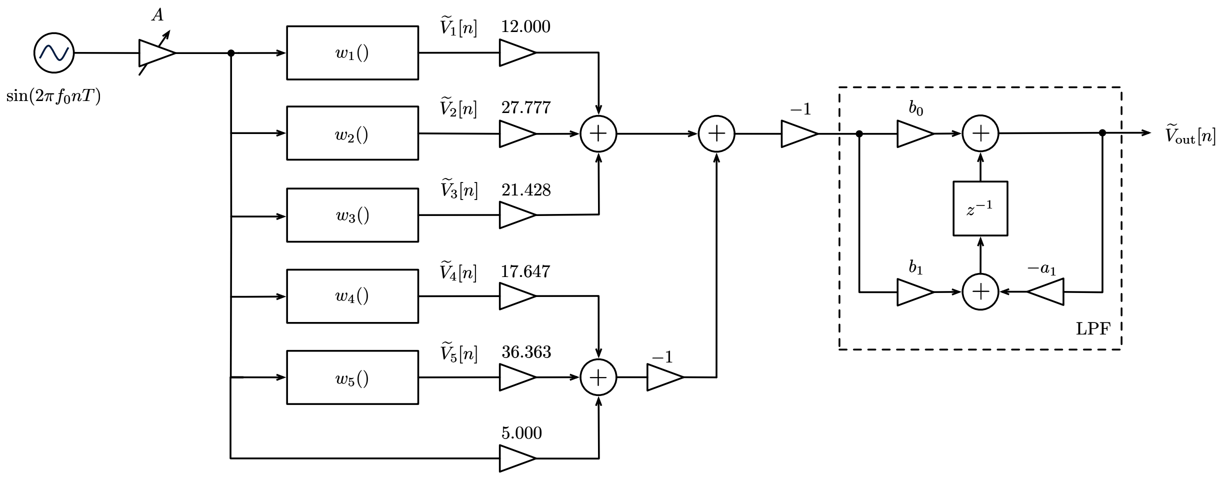

Figure 9: *Block diagram of the proposed digital Buchla 259 wavefolder. The LPF block is the lowpass filter at the output of the system.*

tal model of the wavefolder is derived using nonlinear memoryless mappings based on the input–ouput voltage relationships within the circuit. In an effort to minimize the high levels of aliasing distortion caused by the inherent frequency-expanding behavior of the system, the use of the BLAMP method has been proposed, more specifically in its two-point polynomial form. This method reduces the oversampling requirements of the system, allowing us to accurately process sinusoidal waveforms with fundamental frequencies up to 5 kHz at a sample rate of 352.8 kHz, which is eight times the standard audio rate. The proposed model is free from perceivable aliasing and can be implemented as part of a real-time digital music synthesis environment.

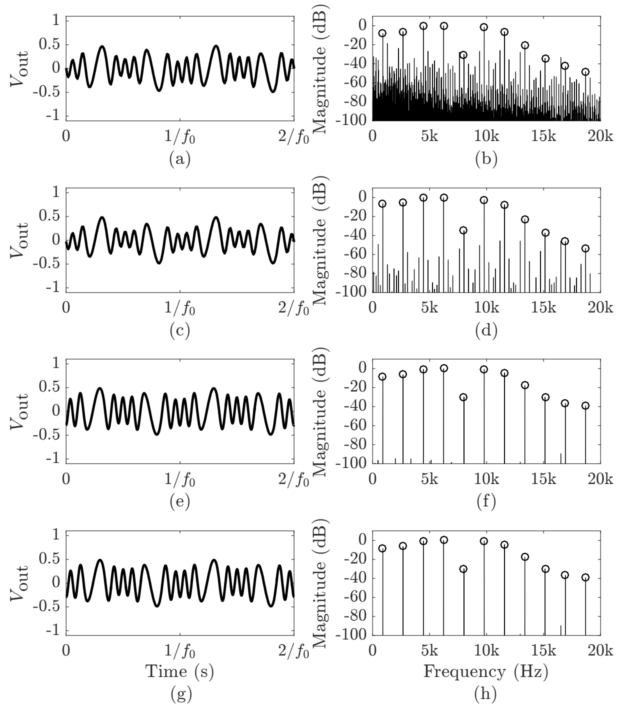

Figure 10: *Waveform and magnitude spectrum of an 890-Hz sinewave ($A = 5$) processed using the proposed model (a)–(b) at audio rate ($f_s = 44.1$ kHz), (c)–(d) at audio rate with the two-point polyBLAMP method, (e)–(f) using 64 times oversampling ($f_s = 2.82$ MHz) and (g)–(h) with 8 times oversampling ($f_s = 352.8$ kHz) and the two-point polyBLAMP method.*

6. ACKNOWLEDGMENTS

The work of Fabián Esqueda is supported by the Aalto ELEC Doctoral School. Part of this work was conducted during Julian Parker's visit to Aalto University in March 2017.

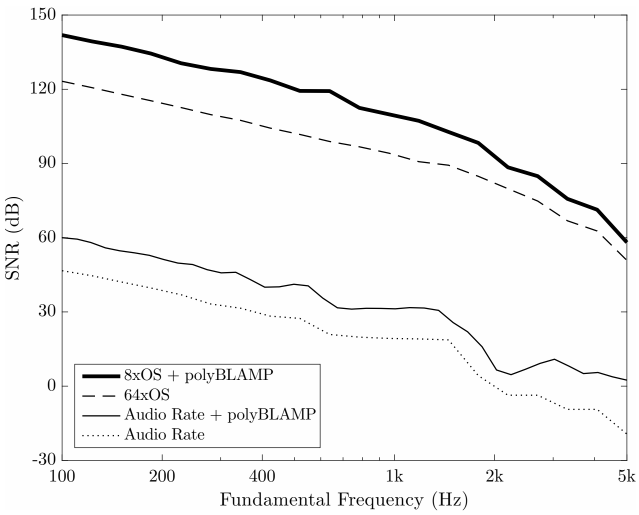

Figure 11: *Measured SNRs for the proposed wavefolder model under sinusoidal input ($A = 5$) implemented trivially ($f_s = 44.1$ kHz), with the two-point polyBLAMP method, with oversampling by factor 64 ($f_s = 2.82$ MHz) and with oversampling by factor 8 and the two-point polyBLAMP method ($f_s = 352.8$ kHz).*

7. REFERENCES

[1] D. Bernstein, *The San Francisco Tape Music Center: 1960s Counterculture and the Avant-Garde*, University of California Press, Ltd., Berkeley, CA, 2008.

[2] Buchla Electronic Musical Instruments, "The history of Buchla," https://buchla.com/history/, Accessed June 19, 2017.

[3] J. Parker and S. D'Angelo, "A digital model of the Buchla lowpass-gate," in *Proc. Int. Conf. Digital Audio Effects (DAFx-13)*, Maynooth, Ireland, Sept. 2013, pp. 278–285.

[4] S. Ciani, "Buchla Concerts 1975," Finders Keepers Records, 2016.

[5] V. Välimäki, F. Fontana, J. O. Smith, and U. Zölzer, "Introduction to the special issue on virtual analog audio effects and musical instruments," *IEEE Trans. Audio, Speech, Language Process.*, vol. 18, no. 4, pp. 713–714, May 2010.

[6] D. Arfib, "Digital synthesis of complex spectra by means of multiplication of non linear distorted sine waves," in *Proc. 59th Conv. Audio Eng. Soc.*, Hamburg, Germany, Mar. 1978.

[7] M. Le Brun, "Digital waveshaping synthesis," *J. Audio Eng. Soc.*, vol. 27, no. 4, pp. 250–266, Apr. 1979.

[8] C. Roads, "A tutorial on non-linear distortion or waveshaping synthesis," *Comput. Music J.*, vol. 3, no. 2, pp. 29–34, 1979.

[9] J. Lane, D. Hoory, E. Martinez, and P. Wang, "Modeling analog synthesis with DSPs," *Comput. Music J.*, vol. 21, no. 4, pp. 23–41, 1997.

[10] J. Chowning, "The synthesis of complex audio spectra by means of frequency modulation," *J. Audio Eng. Soc.*, vol. 21, no. 7, pp. 526–534, Sept. 1973.

[11] V. Lazzarini and J. Timoney, "New perspectives on distortion synthesis for virtual analog oscillators," *Comput. Music J.*, vol. 34, no. 1, 2010.

[12] J. Kleimola, "Audio synthesis by bitwise logical modulation," in *Proc. 11th Int. Conf. Digital Audio Effects (DAFx-08)*, Espoo, Finland, Sept. 2008, pp. 60–70.

[13] J. Kleimola, V. Lazzarini, J. Timoney, and V. Välimäki, "Vector phaseshaping synthesis," in *Proc. 14th Int. Conf. Digital Audio Effects (DAFx-11)*, Paris, France, Sept. 2011, pp. 233–240.

[14] T. Stilson and J. O. Smith, "Analyzing the Moog VCF with considerations for digital implementation," in *Proc. Int. Comput. Music Conf.*, Hong Kong, Aug. 1996, pp. 398–401.

[15] A. Huovilainen, "Non-linear digital implementation of the Moog ladder filter," in *Proc. Int. Conf. Digital Audio Effects (DAFx-04)*, Naples, Italy, Oct. 2004, pp. 61–164.

[16] T. Hélie, "Volterra series and state transformation for real-time simulations of audio circuits including saturations: Application to the Moog ladder filter," *IEEE Trans. Audio, Speech, Language Process.*, vol. 18, no. 4, pp. 747–759, May 2010.

[17] S. D'Angelo and V. Välimäki, "Generalized Moog ladder filter: Part II–explicit nonlinear model through a novel delay-free loop implementation method," *IEEE/ACM Trans. Audio, Speech, Language Process.*, vol. 22, no. 12, pp. 1873–1883, Dec. 2014.

[18] D. Medine, "Dynamical systems for audio synthesis: Embracing nonlinearities and delay-free loops," *Appl. Sci.*, vol. 6, no. 5, 2016.

[19] D. Rossum, "Making digital filters sound analog," in *Proc. Int. Comput. Music Conf.*, San Jose, CA, USA, Oct. 1992, pp. 30–33.

[20] M. Civolani and F. Fontana, "A nonlinear digital model of the EMS VCS3 voltage-controlled filter," in *Proc. Int. Conf. Digital Audio Effects (DAFx-08)*, Espoo, Finland, Sept. 2008, pp. 35–42.

[21] G. Moro and A. P. McPherson, "Approximating non-linear inductors using time-variant linear filters," in *Proc. Int. Conf. Digital Audio Effects (DAFx-15)*, Trondheim, Norway, Nov. 2015, pp. 249–256.

[22] D. T. Yeh, J. Abel, and J. O. Smith III, "Simulation of the diode limiter in guitar distortion circuits by numerical solution of ordinary differential equations," in *Proc. Int. Conf. Digital Audio Effects (DAFx-07)*, Bordeaux, France, Sept. 2007, pp. 197–204.

[23] J. Macak, J. Schimmel, and M. Holters, "Simulation of Fender type guitar preamp using approximation and state-space model," in *Proc. 15th Int. Conf. Digital Audio Effects (DAFx-12)*, York, UK, Sept. 2012, pp. 209–216.

[24] R. C. D. de Paiva, S. D'Angelo, J. Pakarinen, and V. Välimäki, "Emulation of operational amplifiers and diodes in audio distortion circuits," *IEEE Trans. Circuits Syst. II, Exp. Briefs*, vol. 59, no. 10, pp. 688–692, Oct. 2012.

[25] K. J. Werner, V. Nangia, A. Bernardini, J. O. Smith, and A. Sarti, "An improved and generalized diode clipper model for wave digital filters," in *Proc. Audio Eng. Soc. Conv.*, New York, USA, Oct.–Nov. 2015.

[26] A. Bernardini, K. J. Werner, A. Sarti, and J. O. Smith III, "Modeling nonlinear wave digital elements using the Lambert function," *IEEE Transactions on Circuits and Systems I: Regular Papers*, vol. 63, no. 8, pp. 1231–1242, Aug. 2016.

[27] A. Huovilainen, "Enhanced digital models for analog modulation effects," in *Proc. Int. Conf. Digital Audio Effects (DAFx-05)*, Madrid, Spain, Sept. 2005, pp. 155–160.

[28] C. Raffel and J. O. Smith, "Practical modeling of bucket-brigade device circuits," in *Proc. 13th Int. Conf. Digital Audio Effects (DAFx-10)*, Graz, Austria, Sept. 2010, pp. 50–56.

[29] J. Parker, "A simple digital model of the diode-based ring modulator," in *Proc. Int. Conf. Digital Audio Effects (DAFx-11)*, Paris, France, Sept. 2011, pp. 163–166.

[30] H.-M. Lehtonen, J. Pekonen, and V. Välimäki, "Audibility of aliasing distortion in sawtooth signals and its implications for oscillator algorithm design," *J. Acoust. Soc. Am.*, vol. 132, no. 4, pp. 2721–2733, Oct. 2012.

[31] J. Schimmel, "Audible aliasing distortion in digital audio synthesis," *Radioengineering*, vol. 21, no. 1, pp. 56–62, Apr. 2012.

[32] T. Stilson and J. Smith, "Alias-free digital synthesis of classic analog waveforms," in *Proc. Int. Comput. Music Conf.*, Hong Kong, Aug. 1996, pp. 332–335.

[33] E. Brandt, "Hard sync without aliasing," in *Proc. Int. Comput. Music Conf.*, Havana, Cuba, Sept. 2001, pp. 365–368.

[34] V. Välimäki and A. Huovilainen, "Antialiasing oscillators in subtractive synthesis," *IEEE Signal Process. Mag.*, vol. 24, no. 2, pp. 116–125, Mar. 2007.

[35] V. Välimäki, J. Pekonen, and J. Nam, "Perceptually informed synthesis of bandlimited classical waveforms using integrated polynomial interpolation," *J. Acoust. Soc. Am.*, vol. 131, no. 1, pp. 974–986, Jan. 2012.

[36] F. Esqueda, S. Bilbao, and V. Välimäki, "Aliasing reduction in clipped signals," *IEEE Trans. Signal Process.*, vol. 60, no. 20, pp. 5255–5267, Oct. 2016.

[37] F. Esqueda, V. Välimäki, and S. Bilbao, "Rounding corners with BLAMP," in *Proc. Int. Conf. Digital Audio Effects (DAFx-16)*, Brno, Czech Republic, Sept. 2016, pp. 121–128.

[38] J. Parker, V. Zavalishin, and E. Le Bivic, "Reducing the aliasing of nonlinear waveshaping using continuous-time convolution," in *Proc. Int. Conf. Digital Audio Effects (DAFx-16)*, Brno, Czech Republic, Sept. 2016, pp. 137–144.

[39] S. Bilbao, F. Esqueda, J. D. Parker, and V. Välimäki, "Antiderivative antialiasing for memoryless nonlinearities," *IEEE Signal Process. Lett.*, vol. 24, no. 7, pp. 1049–1053, July 2017.

[40] Georgia Institute of Technology, "Aaron Lanterman's Home Page," http://lanterman.ece.gatech.edu/, [Online], Accessed April 9, 2017.

[41] B. Razavi, *Fundamentals of Microelectronics*, Wiley, Hoboken, NJ, 1st edition, 2008.

[42] Intersil, "CA3160 – 4MHz, BiMOS Operational Amplifier with MOSFET Input/CMOS Output," 2004.

[43] Linear Technology, "LTC6087/LTC6088 Dual/Quad 14MHz, Rail-to-Rail CMOS Amplifiers," 2007.

[44] J. O. Smith, *Introduction to Digital Filters with Audio Applications*, W3K Publishing, "http://www.w3k.org/books/", 2007.

[45] V. Zavalishin, *The Art of VA Filter Design*, Native Instruments, Berlin, Germany, 2012.